

# Slantwise convection in the Irminger Sea

I. A.-A. Le Bras<sup>1</sup>, J. Callies<sup>2</sup>, F. Straneo<sup>3</sup>, T.C. Biló<sup>3</sup>, J. Holte<sup>3</sup>, H. L. Johnson<sup>4</sup>

<sup>1</sup>Woods Hole Oceanographic Institution, Woods Hole, MA, USA

<sup>2</sup>California Institute of Technology, Pasadena, CA, USA

<sup>3</sup>Scripps Institution of Oceanography, University of California San Diego, La Jolla, CA, USA

<sup>4</sup>Department of Earth Sciences, University of Oxford, Oxford, UK

## Key Points:

- Down-front wind buoyancy forcing is stronger than heat loss buoyancy forcing in the western Irminger Sea.
- We observe a subsurface ocean response to down-front winds consistent with slantwise convection.
- Slantwise convection may mix waters to several times the conventionally-defined mixed layer depth in this region.

## Abstract

The subpolar North Atlantic is a site of significant carbon dioxide, oxygen, and heat exchange with the atmosphere. This exchange, which regulates transient climate change and prevents large-scale hypoxia throughout the North Atlantic, is thought to be mediated by vertical mixing in the ocean's surface mixed layer. Here we present observational evidence that waters deeper than the conventionally defined mixed layer are affected directly by atmospheric forcing. When northerly winds blow along the Irminger Sea's western boundary current, the Ekman response pushes denser water over lighter water and triggers slantwise convection. We estimate that this down-front wind forcing is four times stronger than air-sea heat flux buoyancy forcing and can mix waters to several times the conventionally defined mixed layer depth. Slantwise convection is not included in most large-scale ocean models, which likely limits their ability to accurately represent subpolar water mass transformations and deep ocean ventilation.

## Plain Language Summary

The deep ocean is an important part of the climate system, as it stores carbon dioxide and heat away from the atmosphere for hundreds to thousands of years. The transfer of properties between the atmosphere and deep ocean is broadly thought to occur in mixed layers formed by cooling at high-latitudes. Here we show that winds blowing in the same direction as ocean currents can trigger slantwise convection, which causes properties to be mixed to several times the conventionally-defined mixed layer depth. We hypothesize that slantwise convection is active in the Irminger Sea as well as in western boundary currents across the subpolar North Atlantic region. We suggest that representing slantwise convection in ocean and climate models may be an important component of reproducing pathways into the deep ocean.

## 1 Introduction

In the high-latitude North Atlantic, warm, salty subtropical waters are transformed into the cold, fresh, oxygen- and carbon-rich waters that fill the deep ocean. The densest waters in the southward flowing lower limb of the Atlantic Meridional Overturning Circulation (AMOC) are Overflow Waters, which form in the Nordic Seas (Dickson & Brown, 1994; Huang et al., 2020), followed by Labrador Sea Water, which forms in deep mixed layers in the central Labrador and Irminger Seas (Yashayaev & Loder, 2016b; de Jong et al., 2018). These waters are observed throughout the deep North Atlantic (Talley & McCartney, 1982; Swift, 1984) and are often thought of as comprising the lower limb of the AMOC.

At the same time, there is growing appreciation that lighter waters formed near ocean boundaries are also a significant component of the AMOC's lower limb (Petit et al., 2020). These lighter waters include, in order of increasing density, eastern Subpolar Mode Waters (Brambilla & Talley, 2008; Brambilla et al., 2008), upper Irminger Sea Intermediate Water (Le Bras et al., 2020), and upper Labrador Sea Water (Pickart et al., 1996). Due to a dearth of year-round observations at the boundaries of the subpolar North Atlantic, however, the pathways and dynamics of this light portion of the AMOC's lower limb remain unclear.

One suggested mechanism of upper Labrador Sea Water formation is slantwise convection. Using an idealized model inspired by a handful of winter vertical density profiles, Straneo and coauthors hypothesized that winds blowing along the Labrador Sea's western boundary current cause an onshore Ekman transport that pushes denser water over lighter water and triggers slantwise convection (Straneo, Kawase, & Pickart, 2002; Straneo, Kawase, & Riser, 2002).

63 Slantwise convection is the response to a mixed convective–shear instability called  
64 symmetric instability and results in mixing approximately along isopycnals (Thomas,  
65 2005; Haine & Marshall, 1998). Evidence of slantwise convection has been observed at  
66 strong currents and persistent fronts such as the Gulf Stream, Kuroshio, and Antarctic  
67 Circumpolar Current (Joyce et al., 2009; Thomas et al., 2013, 2016; Viglione et al., 2018;  
68 Peng et al., 2020) as well as at transient fronts (Thompson et al., 2016; Yu et al., 2019;  
69 Buckingham et al., 2019; Bosse et al., 2021). Slantwise convection is thought to play a  
70 significant role in subtropical mode water formation (Joyce et al., 2013), in the reduction  
71 of the wind-work available to the large-scale ocean circulation (Thomas & Taylor,  
72 2010), and in critically modifying turbulence in the ocean’s surface boundary layer (D’Asaro  
73 et al., 2011). However, its role in the watermass transformations associated with the AMOC  
74 has not yet been demonstrated.

75 The subsurface ocean response to slantwise convection is usefully framed in terms  
76 of potential vorticity (PV). PV is set by atmospheric forcing at the sea surface and is  
77 conserved in the ocean interior in the absence of mixing. So, a water parcel’s PV con-  
78 tains its history of modification. Slantwise convection is triggered when negative PV arises  
79 through a combination of weak vertical buoyancy gradients and strong horizontal buoy-  
80 ancy gradients (or, equivalently, high geostrophic shear) (Hoskins, 1974; Haine & Mar-  
81 shall, 1998; Straneo, Kawase, & Riser, 2002; Giordani et al., 2017). Slantwise convec-  
82 tion homogenizes PV along slanted paths, but does not homogenize density vertically  
83 (Thomas, 2005). Hence, slantwise convection leaves behind a stably stratified surface layer  
84 of homogeneous low PV, just as upright convection creates a layer of weak vertical strat-  
85 ification (Taylor & Ferrari, 2010).

86 Here we present evidence of slantwise convection in the western Irminger Sea from  
87 Overturning in the Subpolar North Atlantic Program (OSNAP) moored observations.  
88 The moorings are located near Cape Farewell, Greenland’s southern tip, where flow dis-  
89 tortions by Greenland’s high topography cause extreme winds (Moore et al., 2008; Harden  
90 & Renfrew, 2012). In the winter and spring the winds are predominantly northerly and  
91 aligned with the Irminger Sea’s southward-flowing western boundary current, which car-  
92 ries cold, fresh Arctic waters on the shelfbreak as well as warm, salty Atlantic Waters  
93 just offshore (Figure 1) (Daniault et al., 2011; Le Bras et al., 2018). These down-front  
94 winds push the denser, saltier water over lighter fresher water and appear to trigger slant-  
95 wise convection (Figure 2). We find that boundary current waters are affected by this  
96 Ekman buoyancy forcing well below the surface mixed layer, suggesting a new mecha-  
97 nism for the transformation and ventilation of the light portion of the AMOC’s lower  
98 limb. Though slantwise convection is likely significant throughout much of the western  
99 subpolar gyre, it is not accounted for in numerical models of this region.

## 100 2 Data and Methods

### 101 2.1 Mooring data and atmospheric reanalysis

102 Our focus is on OSNAP mooring data in the western Irminger Sea at about 60°N  
103 from August 2014 to August 2018. The mooring data are linearly interpolated to a 2 dbar  
104 vertical grid and calibrated using Conductivity, Temperature, Depth (CTD) profiles mea-  
105 sured during research cruises (Le Bras et al., 2018). A low-pass Butterworth filter with  
106 a 40 hour cutoff was applied to all data to remove the tidal signature. The shallowest  
107 instruments on each mooring range from 30 m to 100 m. Upward-facing acoustic Doppler  
108 current profilers (ADCPs) measure the near-surface velocities (Figure 1). Salinity and  
109 temperature are extrapolated by extending the shallowest measured gradient to the sur-  
110 face. This is a sensible approximation in the winter and spring but likely underestimates  
111 the stratification in summer and fall. We use potential temperature and unitless prac-  
112 tical salinity for consistency with past studies. Unless otherwise specified, we consider  
113 all properties and forcing at six-hourly resolution. Our analysis is restricted to 2014 to

114 2018 because an instrument loss on the CF5 mooring, which is the focus of our analy-  
 115 sis, complicates the inclusion of the 2018 to 2020 record. The positions of all moorings  
 116 referred to in this analysis are shown in Figure 1, with the exception of mooring M1, which  
 117 is situated at the 95km mark.

118 Our calculations of the buoyancy flux associated with down-front winds, heat flux,  
 119 and evaporation and precipitation are based on the ERA5 atmospheric reanalysis prod-  
 120 uct. We also analyze ERA5 hourly sea level pressure fields. ERA5 is the fifth genera-  
 121 tion reanalysis product provided by the European Centre for Medium-Range Weather  
 122 Forecast (ECMWF) (Dee et al., 2011), which runs from 1959 to the present. Data are  
 123 provided gridded onto  $0.25^\circ \times 0.25^\circ$  from their original approximately 30 km resolution.  
 124 We bin the hourly data to match the six-hourly mooring data.

## 125 2.2 PV, zonal absolute momentum, and mixed layer definitions

126 We use an across-section reference frame centered around mooring CF5: positive  
 127 velocities are  $11.7^\circ$  clockwise from north. The across-section reference frame was cho-  
 128 sen for the PV calculation as the only horizontal gradients we resolve with the moorings  
 129 are in the along-section direction. Note that this is different from the angle used in Le  
 130 Bras et al. (2018) and Le Bras et al. (2020) ( $23.3^\circ$ ), which was chosen to maximize bound-  
 131 ary current transport.

132 PV is approximated as  $(f+\zeta)N^2-fv_z^2$ , where  $f$  is the Coriolis parameter at  $60^\circ\text{N}$ ,  
 133  $\zeta$  is the relative vorticity of the across-section velocity,  $N^2 = b_z$  is the buoyancy fre-  
 134 quency,  $b = -g\rho_\theta/\rho_0$  is buoyancy,  $g = 9.8 \text{ m s}^{-2}$  is the earth’s gravitational accelera-  
 135 tion,  $\rho_\theta$  is potential density,  $\rho_0 = 1027 \text{ kg m}^{-3}$  is a reference density,  $v$  is across-section  
 136 velocity, and  $z$  subscripts denote vertical derivatives. This form of PV is a good first-  
 137 order approximation and the most complete form of PV that can be calculated from our  
 138 mooring observations. The velocity is smoothed into 100 m vertical bins before gradi-  
 139 ents are calculated from it. We have assumed thermal wind balance,  $fv_z = b_x$ , where  
 140  $b_x$  is the along-section buoyancy gradient. We substitute the horizontal buoyancy gra-  
 141 dient with the vertical shear as horizontal buoyancy gradient measurements in the bound-  
 142 ary current are limited by the continental slope and we find that the observations are  
 143 generally consistent with thermal wind balance.

144 Zonal absolute momentum is calculated as  $m = (f^* - b_x/f)z - fx$ , following Straneo,  
 145 Kawase, and Riser (2002), where  $f^* = 2 \Omega \cos(\text{lat})$ ,  $\Omega = 7.2921 \times 10^{-5} \text{ rad s}^{-1}$  is the  
 146 rotation rate of the earth,  $x$  is distance in the along-section direction and  $z$  is depth. Note  
 147 that our zonal absolute momentum is in the along-section direction, which is nearly but  
 148 not truly zonal.

149 The mixed layer is defined using a threshold of  $\rho = 0.01 \text{ kg m}^{-3}$  relative to the  
 150 potential density at 100 m, as this depth is fairly well-sampled. Mixed layer depths are  
 151 averaged into three-day bins for clarity in the figures, and to highlight mixed layer per-  
 152 sistence.

## 153 2.3 Buoyancy forcing calculations

154 The Ekman buoyancy forcing is given by  $B_{\text{wind}} = -\tau^y b_x / \rho_0 f$ , where  $\tau^y$  is the wind  
 155 stress in the across-section direction. Negative Ekman buoyancy forcing removes buoy-  
 156 ancy from the ocean and is analogous to heat loss. Slantwise convection events are def-  
 157 ined as times when the magnitude of the negative Ekman buoyancy forcing was greater  
 158 than  $7.5 \times 10^{-7} \text{ m}^2 \text{ s}^{-3}$ , which is equivalent to  $-3000 \text{ W m}^{-2}$ . We identified all dates when  
 159 this threshold was surpassed and centered each event around the maximum Ekman buoy-  
 160 ancy forcing. Events were considered separate if the Ekman buoyancy forcing stayed be-  
 161 low the threshold for more than two days.

162 The air–sea heat flux was converted into buoyancy forcing units using  $B_0 = g\alpha Q_{\text{net}}/\rho_0 c_p$ ,  
 163 where  $\alpha$  is the thermal expansion coefficient of seawater with absolute salinity of  $34.9 \text{ g kg}^{-1}$ ,  
 164 conservative temperature of  $4^\circ\text{C}$ , and zero pressure,  $Q_{\text{net}}$  is the air–sea heat loss, and  
 165  $c_p = 3850 \text{ J kg}^{-1} \text{ }^\circ\text{C}^{-1}$  is the specific heat capacity of seawater. Evaporation minus pre-  
 166 cipitation was converted into equivalent buoyancy forcing units using  $B_{e-p} = -g\beta S_{sf c}(E-$   
 167  $P)$ , where  $\beta$  is the haline contraction coefficient calculated using the same parameters  
 168 as  $\alpha$ ,  $S_{sf c}$  is the salinity extrapolated to the surface at the mooring locations, and  $E-$   
 169  $P$  is the evaporation minus precipitation.

170 Our low-PV layer depth analysis is based on an equation derived by Taylor and Fer-  
 171 rari (2010):

$$H(t) = \sqrt{-\frac{2(1 + \epsilon + \gamma)(B_0 + B_{wind})}{N^2 - M^4/f^2}}t, \quad (1)$$

172 where  $H(t)$  is the depth of the low-PV layer;  $\epsilon$  and  $\gamma$  are entrainment coefficients;  $B_0$   
 173 and  $B_{wind}$  are the air–sea and Ekman buoyancy forcing, respectively;  $N$  is the initial ver-  
 174 tical buoyancy frequency; and  $M^2$  is the horizontal buoyancy gradient. The inclusion  
 175 of the horizontal gradient in the denominator accounts for slantwise effects, which mod-  
 176 ify both air–sea and Ekman buoyancy forcing (Straneo, Kawase, & Pickart, 2002).

177 The low-PV layer depth is sensitive to both the temporal resolution of the atmo-  
 178 spheric forcing and the time scale over which the equation is integrated. To remove this  
 179 time dependence, we estimate the ratio of this low-PV layer depth to the convention-  
 180 ally defined mixed layer depth, assuming that the equations for both depths are integrated  
 181 over the same time period:

$$\frac{\text{Low PV layer depth}}{\text{Mixed layer depth}} = \frac{\sqrt{-(B_0 + B_{wind})/(N^2 - M^4/f^2)}}{\sqrt{-B_0/N^2}} \quad (2)$$

182 where we have neglected all entrainment coefficients. Note that these equations assume  
 183 that buoyancy fluxes are negative (acting to deepen the low PV or mixed layer) and ne-  
 184 glect re-stratification. Accordingly, we only calculate this ratio for each time at which  
 185 both the air–sea and Ekman buoyancy forcing are negative, which is about one third of  
 186 the record. We estimate  $N$  as the CF5 vertical buoyancy frequency at 200m and  $M^2$  as  
 187 the horizontal buoyancy gradient at the surface.

### 188 3 Results

#### 189 3.1 Ekman buoyancy forcing

190 The magnitude of the Ekman buoyancy forcing varies significantly across the bound-  
 191 ary current (Figure 3c). This is due to the variation in along-section ( across-front) buoy-  
 192 anc y gradient, which is strongest at CF4 and decreases offshore (Figure 3a). The across-  
 193 section (along-front) wind stress is relatively uniform across the moored array (Figure 3b).  
 194 Both the buoyancy gradient and wind stress are episodic, with more frequent events of  
 195 larger magnitude in the winter. The Ekman buoyancy forcing variability primarily matches  
 196 the wind stress variability, but its strength is modulated by the buoyancy gradient.

197 The buoyancy forcing associated with air–sea heat fluxes and evaporation minus  
 198 precipitation is relatively constant across the moored array (Figure 3d,e). Precipitation,  
 199 which is restratifying and hence a positive buoyancy forcing, dominates in this region;  
 200 evaporation is negligible compared to heat loss. Because our focus is on negative buoy-  
 201 anc y forcing and a direct comparison with heat flux is informative and intuitive, we do  
 202 not include precipitation and evaporation in the rest of our analysis.

203 Negative Ekman buoyancy forcing events can be over ten times stronger than neg-  
 204 ative air–sea heat flux events (Figure 3c,d). In order to compare their net effect over the

205 record, we time-integrate the buoyancy forcing and compare the cumulative negative Ek-  
 206 man buoyancy forcing with the cumulative heat loss buoyancy forcing (Figure 4). Note  
 207 that in order to directly compare with heat loss and for consistency with the low-PV layer  
 208 parameterization, we only include periods of negative buoyancy forcing in this calcula-  
 209 tion.

210 The time-integrated cumulative negative Ekman buoyancy forcing is largest at the  
 211 onshore edge of the boundary current (CF4), where the buoyancy gradients are largest,  
 212 and decreases offshore (Figure 4). At CF4, the cumulative negative Ekman buoyancy  
 213 forcing is 8.5 times stronger than the cumulative air-sea heat flux forcing; at CF5 this  
 214 ratio is 5. On the offshore edge of the boundary current, at CF6 and CF7, the cumu-  
 215 lative negative Ekman buoyancy forcing is comparable to the cumulative air-sea heat  
 216 flux forcing. Overall we find that the cumulative negative Ekman buoyancy forcing is  
 217 about four times larger than the cumulative negative air-sea buoyancy forcing over the  
 218 boundary current (orange and red lines in Figure 4d).

### 219 **3.2 Low-PV layer parameterization**

220 We expect that the significant Ekman buoyancy forcing would trigger slantwise con-  
 221 vection and result in a low-PV layer that is analogous to the mixed layer, but is not nec-  
 222 essarily unstratified in terms of density (Thomas, 2005; Taylor & Ferrari, 2010). This  
 223 low-PV layer can be thought of as the part of the water column affected by surface forc-  
 224 ing. We estimate how the negative Ekman buoyancy forcing modifies the water column,  
 225 relative to the impact of direct air-sea buoyancy forcing, by applying equation 2 for the  
 226 ratio between the low-PV layer depth and the classically defined mixed layer depth.

227 To investigate the impact of all terms on the ratio between the low-PV layer depth  
 228 and the mixed layer depth, we calculate this ratio using only the air-sea buoyancy forc-  
 229 ing, only the Ekman buoyancy forcing, and using both (Figure 5). Our analysis is fo-  
 230 cused on mooring CF5 because it experiences the strongest Ekman buoyancy forcing off-  
 231 shore of the shelfbreak and because lower limb AMOC waters have been observed at this  
 232 site (Le Bras et al., 2020).

233 When only the air-sea buoyancy forcing is included, the ratio is always greater than  
 234 one, because the horizontal density gradient is always positive in the boundary current  
 235 (Figure 5a). In other words, because of slantwise effects, the low-PV layer forced by air-  
 236 sea buoyancy forcing is always deeper than the mixed layer (Straneo, Kawase, & Pickart,  
 237 2002). Our estimate of the ratio of the low-PV layer depth to the mixed layer depth forced  
 238 by air-sea buoyancy flux alone falls between one and two on 95% of days, and has a mean  
 239 value of 1.3 (Figure 5a).

240 When only the Ekman buoyancy forcing is included in equation 1, the ratio of the  
 241 low-PV layer depth to the conventional mixed layer depth can be less than one when the  
 242 air-sea buoyancy forcing is greater than the Ekman buoyancy forcing scaled by the slant-  
 243 wise effect. However, we find that on 42% of the days we consider, the low-PV layer forced  
 244 by Ekman buoyancy forcing is more than two times as deep as the mixed layer. In fact  
 245 the mean value of this ratio considering Ekman buoyancy forcing alone is 3.6, and there  
 246 are a significant number of days on which this ratio is larger than 5 (Figure 5b).

247 Considering both Ekman and air-sea buoyancy forcing (equation 2), we find that  
 248 the low-PV layer is more than two times deeper than the mixed layer on 57% of the days  
 249 we consider, and the mean ratio is 4 (Figure 5c). The distribution is governed by the Ek-  
 250 man buoyancy forcing, particularly for larger ratios. In sum, our analysis suggests that  
 251 there is a low-PV layer in the boundary current that is several times deeper than the con-  
 252 ventionally defined mixed layer, and that its depth is controlled primarily by Ekman buoy-  
 253 ancy forcing.

254

### 3.3 Subsurface ocean response

255

256

257

258

259

260

261

262

263

Our analysis of the expected low-PV layer depth suggests that strong down-front wind events will lead to decreased PV below the conventionally defined mixed layer depth. We find that this is the case within the boundary current (CF5), where dramatic drops in PV are observed in conjunction with strong Ekman buoyancy forcing events (Figure 6). These PV responses are observed well below the conventionally defined mixed layer depth at CF5, which is generally shallower than 300 m, and always shallower than 600 m (Figure 7a). Though some events have a clear response throughout the water column (e.g. late January 2017), the PV time series are noisy. In order to carefully examine the subsurface response to down-front events, we form a composite event.

264

265

266

267

268

We identify 26 individual events in our four-year record. On average, the Ekman buoyancy forcing is elevated for two days (Figure 8a). During this time, the PV decreases throughout the water column at CF5 (Figure 8b,c). The fact that we observe a uniform subsurface PV response in our mooring data is remarkable given that events are identified based primarily on reanalysis wind stress data.

269

270

271

272

273

274

275

276

277

278

The composite event also reveals the evolution of the full boundary current structure in response to down-front winds (Figure 8d–g). At the beginning of the composite event, low salinity waters extend into the core of the boundary current, corresponding to significant horizontal and vertical buoyancy gradients. This is reflected in the high PV over the shelfbreak. Just after the event, the low salinity waters have been pushed onshore and isopycnals have steepened. PV has decreased throughout the shelfbreak area, particularly onshore of CF6, where the Ekman buoyancy forcing is strongest (Figures 3 and 4). Note that PV decreases below the conventionally defined mixed layer over the course of the composite event (green line in Figure 8f,g), consistent with our expectations for slantwise convection.

279

280

281

282

283

284

285

286

287

There is some indication that the PV drops are preceded by an increase in PV (Figure 8a–c), which may be associated with an offshore excursion of the front that would act to increase the magnitude of the Ekman buoyancy forcing. We stress that slantwise convection would result in irreversible mixing regardless of whether there are concurrent frontal excursions. There are also many decreases in PV that are not associated with strong Ekman buoyancy (Figure 6); these may be linked to upstream forcing or frontal excursions. Note that the largest surface heat loss events are less than a tenth the size of the strong Ekman buoyancy forcing events, so the deep PV drops at CF5 are unlikely to be linked to local surface heat loss (Figure 3).

288

289

290

291

292

293

294

295

Zonal absolute momentum is another useful quantity to consider with regards to slantwise convection. When zonal absolute momentum contours are tilted relative to vertical, this indicates that slantwise effects are likely to be significant. After slantwise convection, we expect density surfaces and zonal absolute momentum surfaces to be aligned (Haine & Marshall, 1998; Straneo, Kawase, & Riser, 2002). In our composite event, we find that zonal absolute momentum surfaces are tilted onshore of CF6 and that after the event density and momentum contours are aligned near the surface at CF5 (Figure 8), consistent with slantwise convection at this site.

296

### 3.4 Water mass transformations and property changes

297

298

299

300

301

302

Le Bras et al. (2020) identified a water mass associated with low PV in the Irminger Sea’s western boundary current and called it upper ISIW to distinguish it from the deep ISIW formed in the interior of the basin. They define the upper ISIW density range based on low stratification and a sub-surface salinity maximum in winter: upper ISIW is associated with the transformation of Atlantic Waters of subtropical origin (Le Bras et al., 2020). We now suggest that slantwise convection plays a role in upper ISIW formation.

303 Upper ISIW formation is characterized by both salinity and temperature changes.  
304 Atlantic Waters become denser each year through cooling, and freshen as they mix with  
305 surrounding fresher waters. Hence, the salinity maximum associated with Atlantic Wa-  
306 ters becomes fresher and sinks as it cools each winter (Figure 9b). As the buoyancy gra-  
307 dient between Arctic and subtropical waters is associated with a salinity front, down-  
308 front winds act to mix salinity onshore and downward, i.e. the negative Ekman buoy-  
309 ancy forcing we observe is analogous to brine rejection rather than cooling. At the same  
310 time, as the Atlantic Waters are mixed below the very fresh light waters near the sur-  
311 face, they encounter waters that are of an intermediate saltiness and denser than Atlantic  
312 Waters because they are colder. So, slantwise convection likely plays a multifaceted role  
313 in this seasonal erosion of the Atlantic Water salinity maximum and the mixing of wa-  
314 ters at this complex front.

315 The boundary current freshens significantly towards the end of our four year record  
316 (Figure 9b) (Biló et al., 2022). This results in an overall freshening of the subtropical  
317 Atlantic salinity maximum. Though the previously defined upper ISIW density range  
318 does not thicken seasonally from 2016 to 2018 as much as it did from 2014 to 2016 (black  
319 contours in Figure 9), lighter waters in the boundary current are modified (shoaling grey  
320 contour in Figure 9). In other words, the water mass transformations and mixing pro-  
321 cesses continue in the boundary current, but they occur in lighter, fresher waters than  
322 in past years. We suggest that the upper ISIW density range requires re-evaluation as  
323 properties change interannually, as is done for Labrador Sea Water (Yashayaev & Loder,  
324 2016a).

325 Despite the long-term freshening, we continue to observe subsurface PV responses  
326 to down-front wind events (Figure 6 and Figure 9a). In contrast, the mixed layers off-  
327 shore shoal as the water column freshens (Figure 7). In general, mixed layers are deeper  
328 and more persistent offshore. At CF5, the boundary current maximum, deep mixed lay-  
329 ers are sporadic and there is deepening associated with down-front wind forcing events  
330 that is not seen at CF6. This is likely because upright and slantwise convection are cou-  
331 pled, resulting in some vertical homogenization of density. It is also possible that we over-  
332 estimate the depth of the mixed layer as our observations are subsurface, and that this  
333 calculation is influenced by sub-surface homogeneous layers.

334 In sum, we suggest that slantwise convection plays a role in the seasonal transfor-  
335 mation of Atlantic Waters and find that slantwise convection persists despite the long-  
336 term freshening of Atlantic Waters. This implies that slantwise convection may be more  
337 resilient to freshening than vertical convection is, as long as horizontal density gradients  
338 (and winds) persist.

## 339 4 Discussion

### 340 4.1 Uncertainty

341 There is significant uncertainty in our PV estimate due to the limitations of our  
342 observations. We are only able to calculate the across-section component of relative vor-  
343 ticity, and we apply the thermal wind balance as we resolve vertical gradients better than  
344 horizontal gradients near the continental slope. The most significant source of uncertainty  
345 is the horizontal spacing between the moorings, which limits the horizontal gradients we  
346 can resolve and can lead to aliasing. We estimate that the error in the PV may be up  
347 to several times its calculated value. Our interpretations are hence based primarily on  
348 the temporal evolution of PV rather than its absolute value.

349 The subsurface ocean response is consistent with our expectation that the low-PV  
350 layer is deeper than the mixed layer during down-front wind forcing events. However,  
351 a direct quantification of the low-PV layer from our observations is complicated by the  
352 fact that we do not fully resolve PV. Furthermore, as our observations do not extend to

353 the surface, the mixed layer depths we estimate are potentially an overestimate; the fact  
354 that PV is affected below this upper bound emphasizes that the water column is respond-  
355 ing well below the mixed layer.

356 We would expect to observe areas of negative or zero PV, which are tell-tale signs  
357 of symmetric instability. While the observations are consistent with the presence of these  
358 areas, the moorings do not resolve PV well enough to show this explicitly. The relative  
359 vorticity term ( $\zeta N^2$ ) and the shear term ( $-fv_z^2$ ) both counter the dominant vertical buoy-  
360 ancy gradient term ( $fN^2$ ) within the boundary current (Figure 6) and measuring these  
361 more accurately would likely decrease the PV further.

## 362 4.2 Large-scale context

363 Slantwise convection is forced by extreme wind events, which in this region are usu-  
364 ally associated with cyclones that interact with Greenland's high topography (Doyle &  
365 Shapiro, 1999; Moore & Renfrew, 2005; Josey et al., 2019). A cyclone approaching from  
366 the west would cause southerly winds followed by northerly winds, consistent with our  
367 observation that, during some events, boundary current waters are first pushed offshore  
368 before being pushed back onshore (Figure 8). We find that the peak Ekman buoyancy  
369 forcing of our composite slantwise convection event is associated with a cyclone south-  
370 east of Greenland (Figure 10), suggesting that slantwise convection in this region is largely  
371 driven by synoptic-scale atmospheric features.

372 Our observations, together with the large-scale wind stress, density, and ocean cir-  
373 culation patterns, suggest that slantwise convection could occur all along the east coast  
374 of Greenland and in the western Labrador Sea (Figure 1a). Hence, waters transformed  
375 by slantwise convection in the Irminger Sea may be re-ventilated by slantwise convec-  
376 tion in the Labrador Sea. A similar process likely also occurs in the western Nordic Seas  
377 (Våge et al., 2018). We estimate the relative importance of slantwise and upright con-  
378 vection in the Irminger Sea using our finding that the Ekman buoyancy forcing is four  
379 times the air-sea buoyancy forcing over the boundary current (Figure 1d). To do this,  
380 we define western boundary and interior regions of the Irminger Sea and compare the  
381 total heat flux over both regions with the deduced Ekman buoyancy flux over the west-  
382 ern boundary region (Figure 1a). This back-of-the-envelope calculation suggests that Ek-  
383 man buoyancy fluxes are on the order of the air-sea heat fluxes integrated over the en-  
384 tire Irminger Sea, which is notable given that the basin interior covers a much larger area  
385 than the western boundary region. Slantwise convection may also occur in the interior  
386 of subpolar basins (symmetric instabilities have been observed in open ocean environ-  
387 ments with transient fronts), but we currently lack the observations necessary to quan-  
388 tify this.

389 The water column freshened over the course of our four-year record, causing the  
390 mixed layer depth to decrease offshore of the boundary current (Figures 7 and 9). Slant-  
391 wise convection, however, was more resilient than upright convection to this change; we  
392 observe a deep PV response to down-front winds despite the changing water mass prop-  
393 erties (Figures 6 and 9). We hypothesize that this is because the horizontal density gra-  
394 dient between salty Atlantic-origin and fresh Arctic-origin waters persisted despite the  
395 freshening of the Atlantic-origin waters. As freshwater sources to the subpolar North At-  
396 lantic increase, we may find an increasing role for slantwise convection relative to up-  
397 right convection. However, we note that there is likely important interplay between up-  
398 right and slantwise convection. The stratification is low in this region due to upright con-  
399 vection, which is important pre-conditioning that makes the water column generally sus-  
400 ceptible to slantwise convection. Furthermore, during a down-front wind event, the ini-  
401 tial response to the Ekman buoyancy forcing may be upright convection, which then trig-  
402 gers symmetric instability and finally adjustment via slantwise convection.

### 4.3 Outlook for modeling and observations

Although it is possible to parameterize slantwise convection in numerical models, successful implementation requires that sharp horizontal density gradients are resolved (Thomas, 2005; Thomas & Lee, 2005; Bachman et al., 2017). Gula et al. (2014) found that even with 500 m horizontal resolution, they did not fully resolve symmetric instability in the Gulf Stream region, and Dong et al. (2021) estimated that  $\approx 100$  m horizontal scales need to be resolved to simulate symmetric instability in the subpolar boundary regions. The salinity fronts of the subpolar North Atlantic present a particular challenge as most ocean models are prone to salinity drifts and do not reliably simulate fresh water fluxes from Greenland and the Arctic (Danabasoglu et al., 2016; Dukhovskoy et al., 2016; Böning et al., 2016).

Field campaigns elsewhere have resolved the horizontal structure of PV during down-front wind events using towed instruments and gliders (Joyce et al., 2009; Thomas et al., 2013, 2016; Adams et al., 2017; Yu et al., 2019; Thompson et al., 2016; Carpenter et al., 2020; Peng et al., 2020; Bosse et al., 2021). Given the harsh conditions in the Irminger Sea, a winter glider survey is the most promising avenue for better resolving this process in the future. Previous studies have observed the subduction of high oxygen and high chlorophyll waters associated with down-front wind-forced instabilities (Joyce et al., 2009; Thomas et al., 2013; Bosse et al., 2021). This implies that slantwise convection may be an important contributor to the ventilation of the deep Atlantic. Oxygen sensors were deployed on the Irminger and Labrador Sea OSNAP moorings in the summer of 2020. The resulting data will provide valuable information on the coupling of water mass transformation via slantwise convection with ventilation and biogeochemical cycling.

## 5 Conclusions

We have presented observational evidence consistent with slantwise convection in the Irminger Sea’s western boundary current. Strong winds blowing in the same direction as the current push denser waters onshore over lighter waters and trigger slantwise convection (Figure 2). Over our four-year record, we identified 26 down-front wind forcing events, which coincide with a subsurface decrease in PV below the conventionally defined surface mixed layer (Figure 8). We estimate that the Ekman buoyancy forcing is four times as strong as the air–sea buoyancy forcing over the boundary current (Figure 4), and that slantwise convection impacts the water column to four times the conventionally defined mixed layer depth on average (Figure 5).

Interestingly, the down-front winds push saltier water over fresher water, and are hence analogous to evaporation or brine rejection rather than cooling. Since slantwise convection necessarily brings fresh continental shelf waters into contact with saltier denser waters of a different origin, proper representation of salinity fronts and slantwise convection in ocean models will likely improve their representation of subpolar water mass transformations, as well as associated carbon and heat fluxes.

## Data Availability

OSNAP mooring data used in this study are available at <http://www.o-snap.org/observations/data/> under “US East Cape Farewell Slope Array”. ERA5 reanalysis hourly data was downloaded from <https://cds.climate.copernicus.eu/cdsapp#!/dataset/reanalysis-era5-single-levels>. Hourly wind stress and heat flux fields were downloaded on June 18, 2020 and hourly sea level pressure data was downloaded on July 13, 2021. ERA5 monthly wind stress fields shown in Figure 1 were downloaded on August 4, 2020 from <https://cds.climate.copernicus.eu/cdsapp#!/dataset/reanalysis-era5-single-levels-monthly-means>. Monthly sea surface height (anomaly) data (Figure 1) are Ssalto/Duacs altimeter products distributed by Aviso+ with support from Cnes

452 and by the Copernicus Marine and Environment Monitoring Service (CMEMS). They  
 453 were downloaded on August 31, 2020 from [https://resources.marine.copernicus.eu/  
 454 product-detail/SEALEVEL\\_GLO\\_PHY\\_L4\\_MY\\_008\\_047](https://resources.marine.copernicus.eu/product-detail/SEALEVEL_GLO_PHY_L4_MY_008_047).

### 455 Acknowledgments

456 ILB, FS, TCB, and JH gratefully acknowledge the US National Science Foundation (NSF):  
 457 this work was supported by grants OCE-1258823, OCE-1756272, OCE-1948335, and OCE-  
 458 2038481. JC gratefully acknowledges NSF support through grant OCE-1924354. HLJ  
 459 was supported by the SNAP-DRAGON program (UK Natural Environment Research  
 460 Council grant number NE/T013494/1). We gratefully acknowledge the many scientists  
 461 and mariners who went to sea to collect the observational data, and Bob Pickart in par-  
 462 ticular.

### 463 References

- 464 Adams, K. A., Hosegood, P., Taylor, J. R., Sallée, J. B., Bachman, S., Torres, R.,  
 465 & Stamper, M. (2017). Frontal circulation and submesoscale variability dur-  
 466 ing the formation of a southern ocean mesoscale eddy. *Journal of Physical  
 467 Oceanography*, *47*, 1737–1753. doi: 10.1175/JPO-D-16-0266.1
- 468 Bachman, S. D., Fox-Kemper, B., Taylor, J. R., & Thomas, L. N. (2017). Param-  
 469 eterization of Frontal Symmetric Instabilities. I: Theory for Resolved Fronts.  
 470 *Ocean Modelling*, *109*, 72–95. doi: 10.1016/j.ocemod.2016.12.003
- 471 Biló, T. C., Straneo, F., Holte, J., & Le Bras, I. A. (2022). Arrival of New Great  
 472 Salinity Anomaly Weakens Convection in the Irminger Sea. *Geophysical Re-  
 473 search Letters*, *49*, e2022GL098857. doi: 10.1029/2022gl098857
- 474 Böning, C. W., Behrens, E., Biastoch, A., Getzlaff, K., & Bamber, J. L. (2016).  
 475 Emerging impact of Greenland meltwater on deepwater formation in the North  
 476 Atlantic Ocean. *Nature Geoscience*, *9*, 523–527. doi: 10.1038/ngeo2740
- 477 Bosse, A., Testor, P., Damien, P., Estournel, C., Marsaleix, P., Mortier, L., ... Tail-  
 478 landier, V. (2021). Wind-Forced Submesoscale Symmetric Instability around  
 479 Deep Convection in the Northwestern Mediterranean Sea. *Fluids*, *6*, 1–27. doi:  
 480 10.3390/fluids603012
- 481 Brambilla, E., & Talley, L. D. (2008). Subpolar Mode Water in the northeastern  
 482 Atlantic: 1. Averaged properties and mean circulation. *Journal of Geophysical  
 483 Research*, *113*, C04025. doi: 10.1029/2006JC004062
- 484 Brambilla, E., Talley, L. D., & Robbins, P. E. (2008). Subpolar Mode Water in  
 485 the northeastern Atlantic: 2. Origin and transformation. *Journal of Geophysi-  
 486 cal Research*, *113*, C04026. doi: 10.1029/2006JC004063
- 487 Buckingham, C. E., Lucas, N. S., Belcher, S. E., Rippeth, T. P., Grant, A. L., Le  
 488 Sommer, J., ... Naveira Garabato, A. C. (2019). The Contribution of Surface  
 489 and Submesoscale Processes to Turbulence in the Open Ocean Surface Bound-  
 490 ary Layer. *Journal of Advances in Modeling Earth Systems*, *11*, 4066–4094.  
 491 doi: 10.1029/2019MS001801
- 492 Carpenter, J. R., Rodrigues, A., Schultze, L. K., Merckelbach, L. M., Suzuki, N.,  
 493 Baschek, B., & Umlauf, L. (2020). Shear Instability and Turbulence Within  
 494 a Submesoscale Front Following a Storm. *Geophysical Research Letters*, *47*,  
 495 e2020GL090365. doi: 10.1029/2020GL090365
- 496 Danabasoglu, G., Yeager, S. G., Kim, W. M., Behrens, E., Bentsen, M., Bi, D., ...  
 497 Yashayaev, I. (2016). North Atlantic simulations in Coordinated Ocean-ice  
 498 Reference Experiments phase II (CORE-II). Part II: Inter-annual to decadal  
 499 variability. *Ocean Modelling*, *97*, 65–90. doi: 10.1016/j.ocemod.2015.11.007
- 500 Daniault, N., Lherminier, P., & Mercier, H. (2011). Circulation and Transport at the  
 501 Southeast Tip of Greenland. *Journal of Physical Oceanography*, *41*, 437–457.  
 502 doi: 10.1175/2010JPO4428.1

- 503 D'Asaro, E., Lee, C., Rainville, L., Harcourt, R., & Thomas, L. (2011). Enhanced  
504 turbulence and energy dissipation at ocean fronts. *Science*, *332*, 318–322. doi:  
505 10.1126/science.1201515
- 506 Dee, D. P., Uppala, S. M., Simmons, A. J., Berrisford, P., Poli, P., Kobayashi, S., ...  
507 Vitart, F. (2011). The ERA-Interim reanalysis: configuration and performance  
508 of the data assimilation system. *Quarterly Journal of the Royal Meteorological  
509 Society*, *137*, 553–597. doi: 10.1002/qj.828
- 510 de Jong, M. F., Oltmanns, M., Karstensen, J., & De Steur, L. (2018). Deep convec-  
511 tion in the Irminger Sea observed with a dense mooring array. *Oceanography*,  
512 *31(1)*, 50–59. doi: 10.5670/oceanog.2018.109
- 513 Dickson, R. R., & Brown, J. (1994). The production of North Atlantic Deep Wa-  
514 ter: Sources, rates, and pathways. *Journal of Geophysical Research: Oceans*,  
515 *99*, 12319–12341. doi: 10.1029/94JC00530
- 516 Dong, J., Fox-Kemper, B., Zhang, H., & Dong, C. (2021). The Scale and Activity  
517 of Symmetric Instability Estimated from a Global Submesoscale-Permitting  
518 Ocean Model. *Journal of Physical Oceanography*, *51*, 1655–1670. doi:  
519 10.1175/JPO-D-20-0159.1
- 520 Doyle, J. D., & Shapiro, M. A. (1999). Flow response to large-scale topography: the  
521 Greenland tip jet. *Tellus A*, *51*, 728–748. doi: 10.1034/j.1600-0870.1996.00014  
522 .x
- 523 Dukhovskoy, D. S., Myers, P. G., Platov, G., Timmermans, M., Curry, B.,  
524 Proshutinsky, A., ... Somavilla, R. (2016). Greenland freshwater path-  
525 ways in the sub-Arctic Seas from model experiments with passive tracers.  
526 *Journal of Geophysical Research: Oceans*, *121*, 877–907. doi: 10.1002/  
527 2015JC011290@10.1002/(ISSN)2169-9291.FAMOS1
- 528 Giordani, H., Lebeaupin-Brossier, C., Léger, F., & Caniaux, G. (2017). A PV-  
529 approach for dense water formation along fronts: Application to the North-  
530 western Mediterranean. *Journal of Geophysical Research: Oceans*, *122*, 995–  
531 1015. doi: 10.1002/2016JC012019
- 532 Gula, J., Molemaker, J. J., & McWilliams, J. C. (2014). Submesoscale Cold Fila-  
533 ments in the Gulf Stream. *Journal of Physical Oceanography*, *44*, 2617–2643.  
534 doi: 10.1175/JPO-D-14-0029.1
- 535 Haine, T. W., & Marshall, J. (1998). Gravitational, symmetric, and baroclinic in-  
536 stability of the ocean mixed layer. *Journal of Physical Oceanography*, *28*, 634–  
537 658. doi: 10.1175/1520-0485(1998)028<0634:GSABIO>2.0.CO;2
- 538 Harden, B. E., & Renfrew, I. A. (2012). On the spatial distribution of high winds  
539 off southeast Greenland. *Geophysical Research Letters*, *39*. doi: 10.1029/  
540 2012GL052245
- 541 Hoskins, B. J. (1974). The role of potential vorticity in symmetric stability and in-  
542 stability. *Quarterly Journal of the Royal Meteorological Society*, *100*, 480–482.  
543 doi: 10.1093/cdj/3.1.2
- 544 Huang, J., Pickart, R. S., Huang, R. X., Lin, P., Brakstad, A., & Xu, F. (2020).  
545 Sources and upstream pathways of the densest overflow water in the Nordic  
546 Seas. *Nature Communications*, *11*, 1–9. doi: 10.1038/s41467-020-19050-y
- 547 Josey, S. A., de Jong, M. F., Oltmanns, M., Moore, G. K., & Weller, R. A. (2019).  
548 Extreme Variability in Irminger Sea Winter Heat Loss Revealed by Ocean Ob-  
549 servatories Initiative Mooring and the ERA5 Reanalysis. *Geophysical Research  
550 Letters*, *46*, 293–302. doi: 10.1029/2018GL080956
- 551 Joyce, T. M., Thomas, L. N., & Bahr, F. (2009). Wintertime observations of Sub-  
552 tropical Mode Water formation within the Gulf Stream. *Geophysical Research  
553 Letters*, *36*, n/a—n/a. doi: 10.1029/2008GL035918
- 554 Joyce, T. M., Thomas, L. N., Dewar, W. K., & Garton, J. B. (2013). Eighteen De-  
555 gree Water formation within the Gulf Stream during CLIMODE. *Deep-Sea Re-  
556 search Part II: Topical Studies in Oceanography*, *91*, 1–10. doi: 10.1016/j.dsr2  
557 .2013.02.019

- 558 Le Bras, I., Straneo, F., Holte, J., de Jong, M. F., & Holliday, N. P. (2020). Rapid  
559 Export of Waters Formed by Convection Near the Irminger Sea's Western  
560 Boundary. *Geophysical Research Letters*, *47*. doi: 10.1029/2019GL085989
- 561 Le Bras, I., Straneo, F., Holte, J., & Holliday, N. P. (2018). Seasonality of Freshwa-  
562 ter in the East Greenland Current System From 2014 to 2016. *Journal of Geo-  
563 physical Research: Oceans*, *123*. doi: 10.1029/2018JC014511
- 564 Moore, G. W. K., Pickart, R. S., & Renfrew, I. A. (2008). Buoy observations from  
565 the windiest location in the world ocean, Cape Farewell, Greenland. *Geophysi-  
566 cal Research Letters*, *35*, 3–7. doi: 10.1029/2008GL034845
- 567 Moore, G. W. K., & Renfrew, I. A. (2005). Tip jets and barriers winds: A  
568 QuickSCAT climatology of high wind speed events around greenland. *Journal  
569 of Climate*, *18*, 4919. doi: 10.1175/JCLI9007.1
- 570 Peng, J. P., Holtermann, P., & Umlauf, L. (2020). Frontal instability and energy dis-  
571 sipation in a submesoscale upwelling filament. *Journal of Physical Oceanogra-  
572 phy*, *50*, 2017–2035. doi: 10.1175/JPO-D-19-0270.1
- 573 Petit, T., Lozier, M. S., Josey, S. A., & Cunningham, S. A. (2020). Atlantic Deep  
574 Water Formation Occurs Primarily in the Iceland Basin and Irminger Sea  
575 by Local Buoyancy Forcing. *Geophysical Research Letters*, *47*, 1–9. doi:  
576 10.1029/2020GL091028
- 577 Pickart, R. S., Smethie, W. M., Lazier, J. R. N., Jones, E. P., & Jenkins, W. J.  
578 (1996). Eddies of newly formed upper Labrador Sea water. *Journal of Geo-  
579 physical Research: Oceans*, *101*, 20711–20726. doi: 10.1029/96JC01453
- 580 Straneo, F., Kawase, M., & Pickart, R. S. (2002). Effects of Wind on Con-  
581 vection in Strongly and Weakly Baroclinic Flows with Application to the  
582 Labrador Sea. *Journal of Physical Oceanography*, *32*, 2603–2618. doi:  
583 10.1175/1520-0485-32.9.2603
- 584 Straneo, F., Kawase, M., & Riser, S. C. (2002). Idealized models of slantwise convec-  
585 tion in a baroclinic flow. *Journal of Physical Oceanography*, *32*, 558–572. doi:  
586 10.1175/1520-0485(2002)032<0558:IMOSCI>2.0.CO;2
- 587 Swift, J. H. (1984). The circulation of the Denmark Strait and Iceland-Scotland  
588 overflow waters in the North Atlantic. *Deep Sea Research*, *31*, 1339–1355. doi:  
589 10.1016/0198-0149(84)90005-0
- 590 Talley, L. D., & McCartney, M. S. (1982). Distribution and circulation of Labrador  
591 Sea Water. *Journal of Physical Oceanography*, *12*, 1189–1205. doi: 10.1175/  
592 1520-0485(1982)012(1189:DACOLS)2.0.CO;2
- 593 Taylor, J. R., & Ferrari, R. (2010). Buoyancy and wind-driven convection at mixed  
594 layer density fronts. *Journal of Physical Oceanography*, *40*, 1222–1242. doi: 10  
595 .1175/2010JPO4365.1
- 596 Thomas, L. N. (2005). Destruction of Potential Vorticity by Winds. *Journal of  
597 Physical Oceanography*, *35*, 2457–2466. doi: 10.1175/JPO2830.1
- 598 Thomas, L. N., & Lee, C. M. (2005). Intensification of ocean fronts by down-  
599 front winds. *Journal of Physical Oceanography*, *35*, 1086–1102. doi:  
600 10.1175/JPO2737.1
- 601 Thomas, L. N., & Taylor, J. R. (2010). Reduction of the usable wind-work on the  
602 general circulation by forced symmetric instability. *Geophysical Research Let-  
603 ters*, *37*. doi: 10.1029/2010GL044680
- 604 Thomas, L. N., Taylor, J. R., D'Asaro, E. A., Lee, C. M., Klymak, J. M., &  
605 Shcherbina, A. (2016). Symmetric instability, inertial oscillations, and turbu-  
606 lence at the gulf stream front. *Journal of Physical Oceanography*, *46*, 197–217.  
607 doi: 10.1175/JPO-D-15-0008.1
- 608 Thomas, L. N., Taylor, J. R., Ferrari, R., & Joyce, T. M. (2013). Symmetric in-  
609 stability in the Gulf Stream. *Deep-Sea Research Part II: Topical Studies in  
610 Oceanography*, *91*, 96–110. doi: 10.1016/j.dsr2.2013.02.025
- 611 Thompson, A. F., Lazar, A., Buckingham, C., Garabato, A. C., Damerell, G. M., &  
612 Heywood, K. J. (2016). Open-ocean submesoscale motions: A full seasonal cy-

- 613 cle of mixed layer instabilities from gliders. *Journal of Physical Oceanography*,  
614 *46*, 1285–1307. doi: 10.1175/JPO-D-15-0170.1
- 615 Våge, K., Papritz, L., Håvik, L., Spall, M. A., & Moore, G. W. (2018). Ocean  
616 convection linked to the recent ice edge retreat along east Greenland. *Nature*  
617 *Communications* *2018 9:1*, *9*, 1–8. doi: 10.1038/s41467-018-03468-6
- 618 Viglione, G. A., Thompson, A. F., Flexas, M. M., Sprintall, J., Swart, S., Viglione,  
619 G. A., . . . Swart, S. (2018). Abrupt Transitions in Submesoscale Structure in  
620 Southern Drake Passage: Glider Observations and Model Results. *Journal of*  
621 *Physical Oceanography*, *48*, 2011–2027. doi: 10.1175/JPO-D-17-0192.1
- 622 Yashayaev, I., & Loder, J. W. (2016a). Further intensification of deep convection  
623 in the Labrador Sea in 2016. *Geophysical Research Letters*, *44*. doi: 10.1002/  
624 2013GL058740.Received
- 625 Yashayaev, I., & Loder, J. W. (2016b). Recurrent replenishment of Labrador Sea  
626 Water and associated decadal-scale variability. *Journal of Geophysical Re-*  
627 *search: Oceans*, *121*, 8095–8114. doi: 10.1002/2016JC012046
- 628 Yu, X., Naveira Garabato, A. C., Martin, A. P., Evans, D. G., & Su, Z. (2019).  
629 Wind-Forced Symmetric Instability at a Transient Mid-Ocean Front. *Geophys-*  
630 *ical Research Letters*, *46*, 11281–11291. doi: 10.1029/2019GL084309

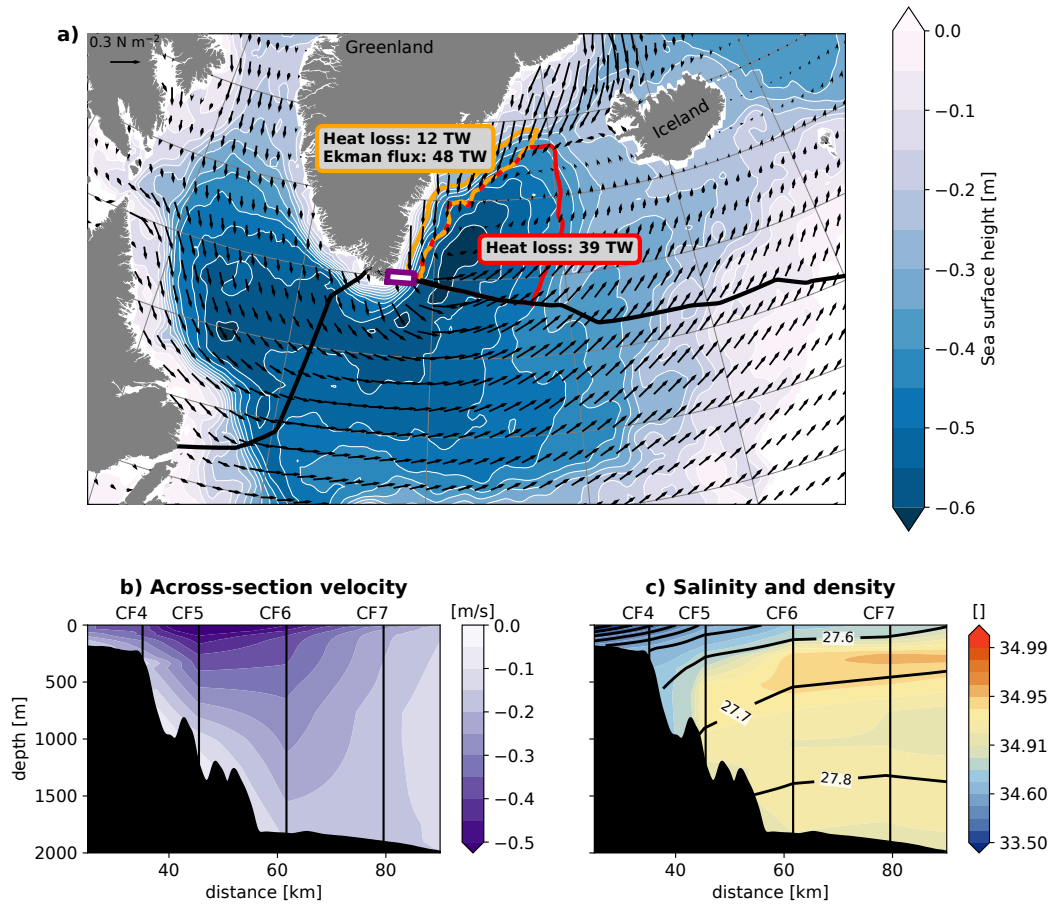


**Figure 1.** Regional context in winter and spring. All quantities in panels a–c are averaged over November–April, 2014–2018. **a)** Wind stress (arrows) and sea surface height (contours) in the subpolar North Atlantic. The black line is the OSNAP section and the purple box highlights the Cape Farewell moorings shown in panels b and c. The red and orange lines indicate the Irminger interior and boundary regions bounded by the 2000m and 500m isobaths; they are labelled with their time-mean spatially-integrated air–sea heat flux loss and the deduced equivalent Ekman heat flux loss in the boundary region. **b)** Across-mooring-line velocity measured by the moorings. **c)** Observed salinity, shown with  $\sigma_\theta$  isopycnals separated by  $0.1 \text{ kg m}^{-3}$ . The labeled vertical black lines in b and c indicate mooring positions.

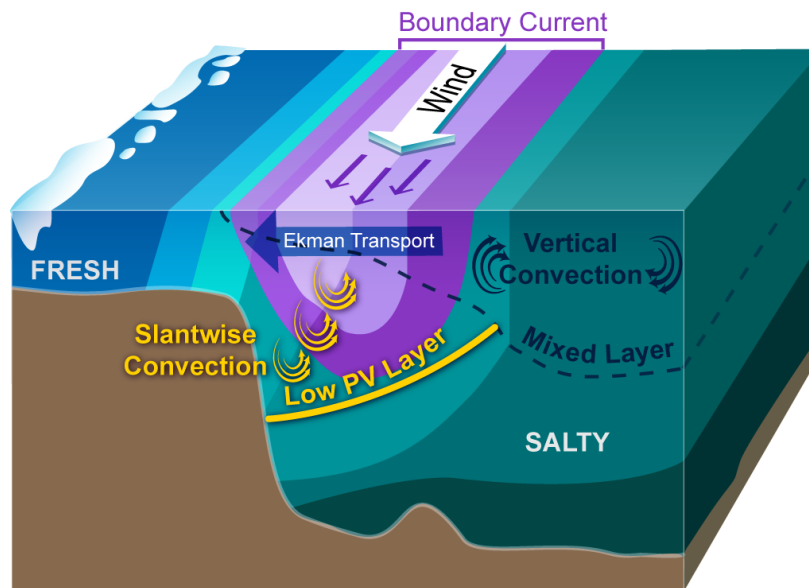


**Figure 2.** Schematic illustration of hypothesized slantwise convection in the Irminger Sea. Purple contours represent boundary current velocity, and blue–green contours represent density layers. Winds blowing in the same direction as the boundary current push salty, denser water over fresh, lighter water through the Ekman response. This triggers slantwise convection, which mixes water along slanted paths and creates a low-PV layer that is several times deeper than the mixed layer in the boundary current. The unstratified mixed layer, formed via cooling and upright convection, is deeper offshore.

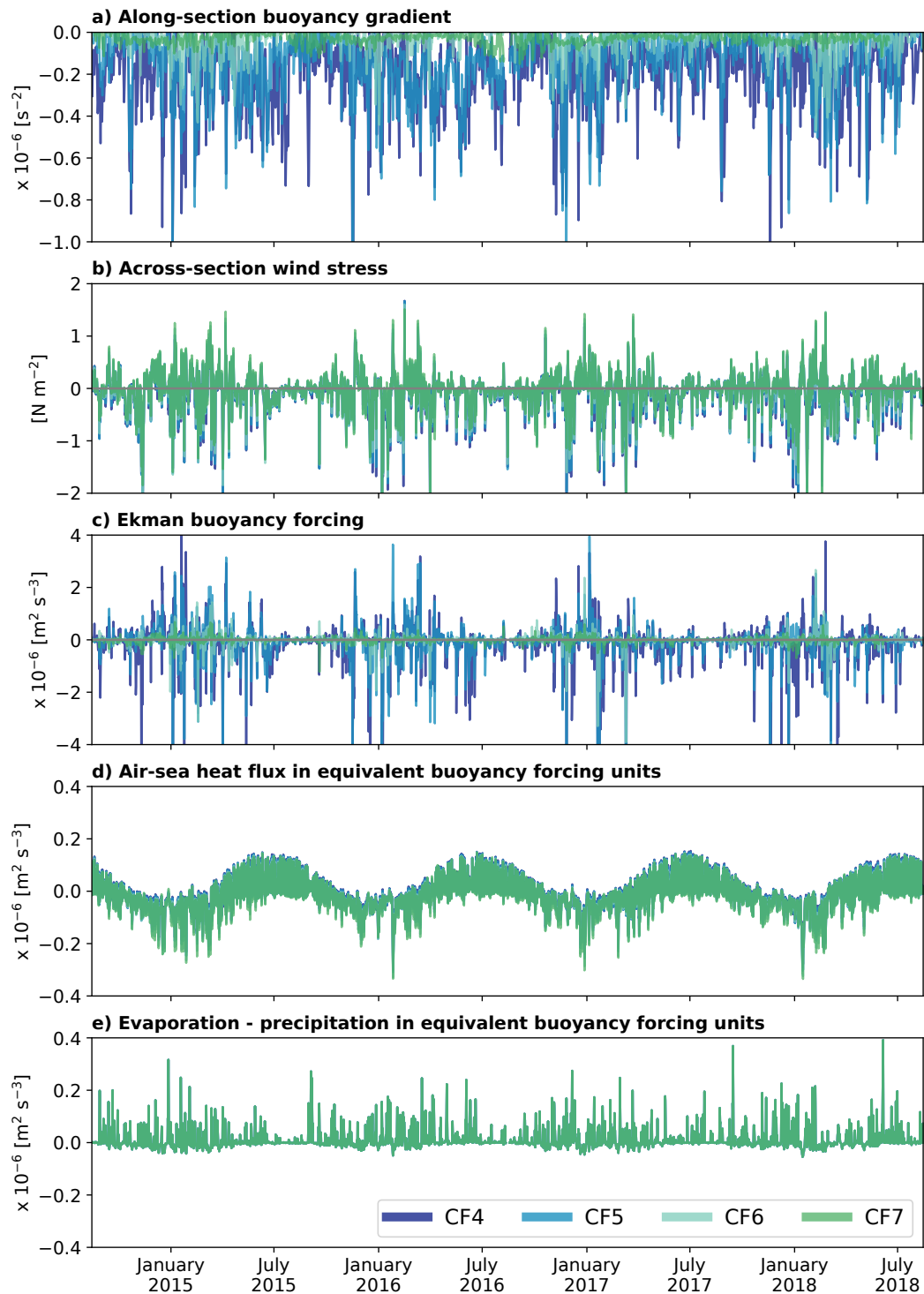


**Figure 3.** Buoyancy forcing and its components at the boundary current moorings (CF4–7) as labeled. The Ekman buoyancy forcing (panel c), is proportional to the product of the buoyancy gradient and wind stress (panels a and b, respectively). Note that the y-axes in panels d and e have one tenth of the range of panel c.

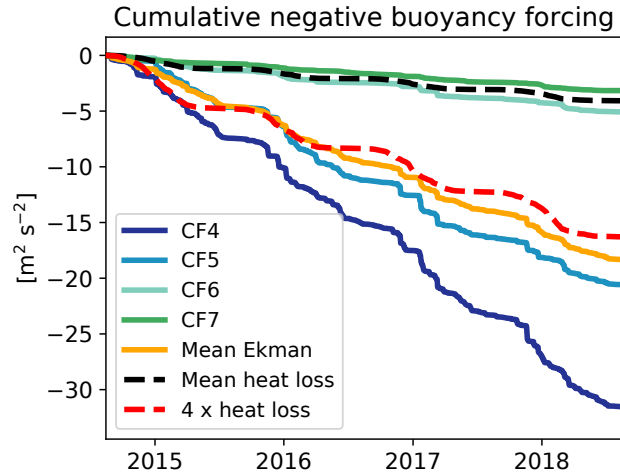


**Figure 4.** Cumulative negative Ekman buoyancy forcing (solid lines) estimated at the boundary current moorings, and the boundary current average (orange), shown with the cumulative negative buoyancy forcing associated with air–sea heat fluxes averaged over the boundary current (black dashed) as well as four times the air–sea heat fluxes for reference (red dashed).

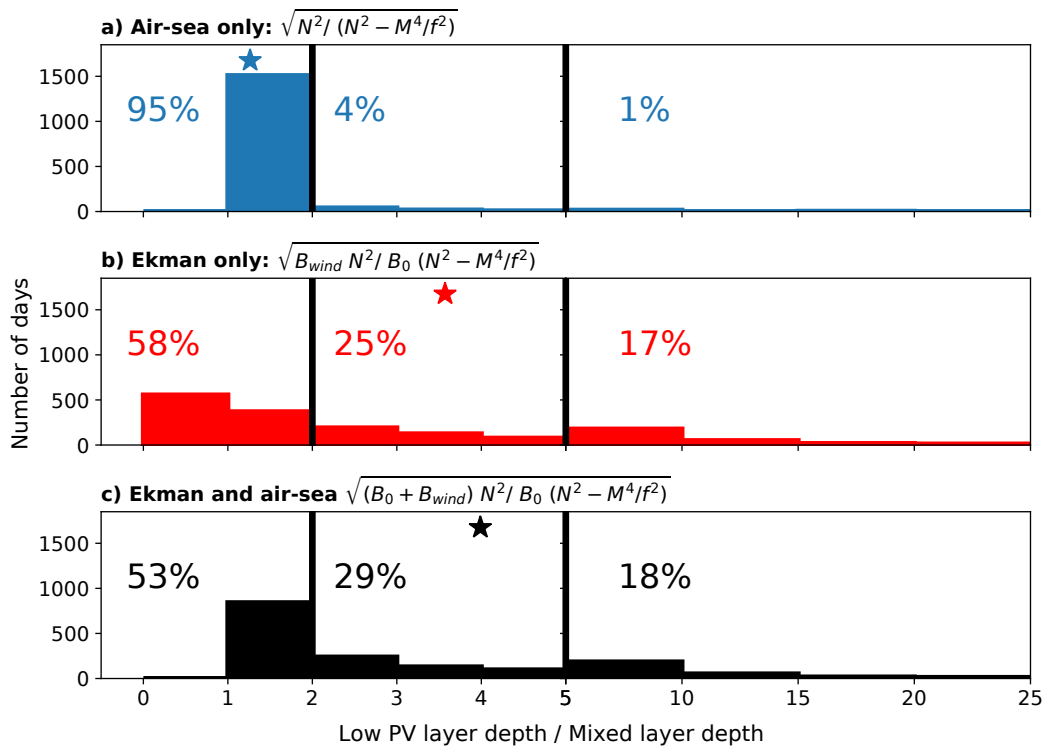


**Figure 5.** Histogram of the ratio of the depth of the low-PV layer formed via slantwise convection to the conventionally derived mixed layer depth. The distribution of the ratio within the boundary current (CF5) is shown, based on observed air–sea and wind forcing and vertical and horizontal density gradients. The fraction of days for which the ratio is less than 2, between 2 and 5, and greater than 5 is noted. Stars indicate the mean ratio for each forcing configuration. The horizontal axis and bin size changes at a ratio of 5.

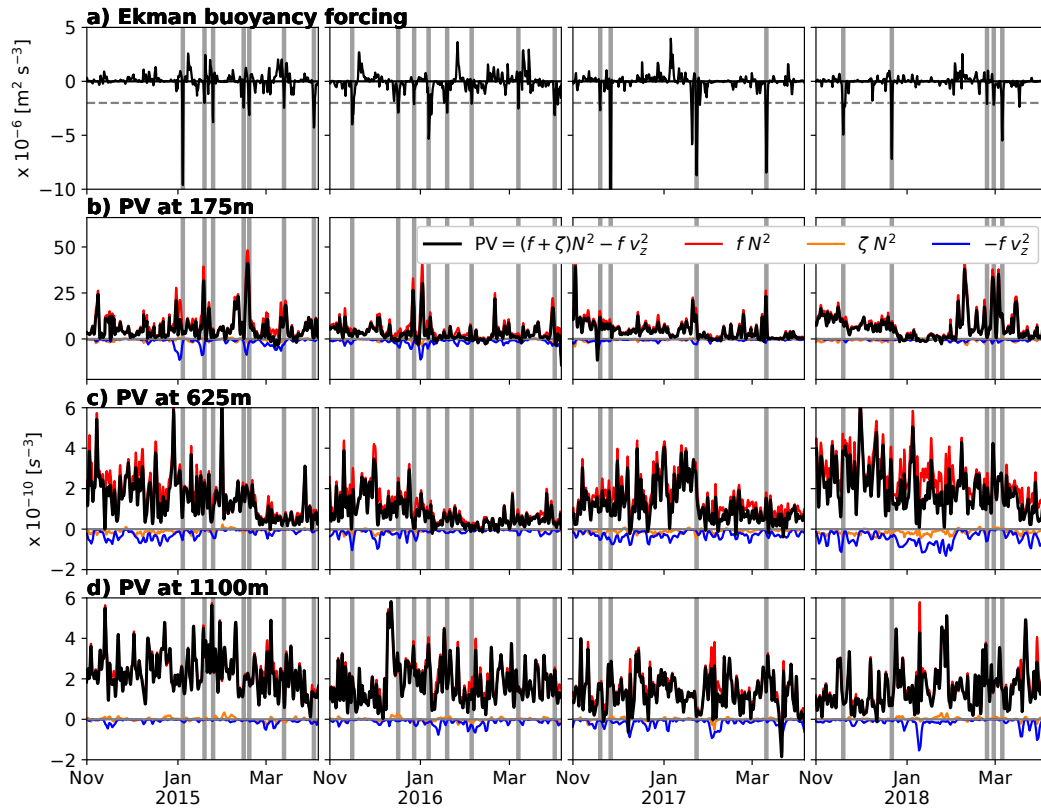


**Figure 6.** Atmospheric forcing and deep ocean response at the boundary current maximum, CF5, from November to April, 2014–2018. **a)** Ekman buoyancy forcing; grey shaded areas in all panels indicate times at which the magnitude of the negative Ekman buoyancy forcing exceeds  $7.5 \times 10^{-7} \text{ m}^2 \text{ s}^{-3}$  (horizontal dotted line). **b, c, d)** PV and its components at 175 m, 625 m and 1100 m respectively. Strong down-front wind forcing events are associated with drops in PV throughout the water column.

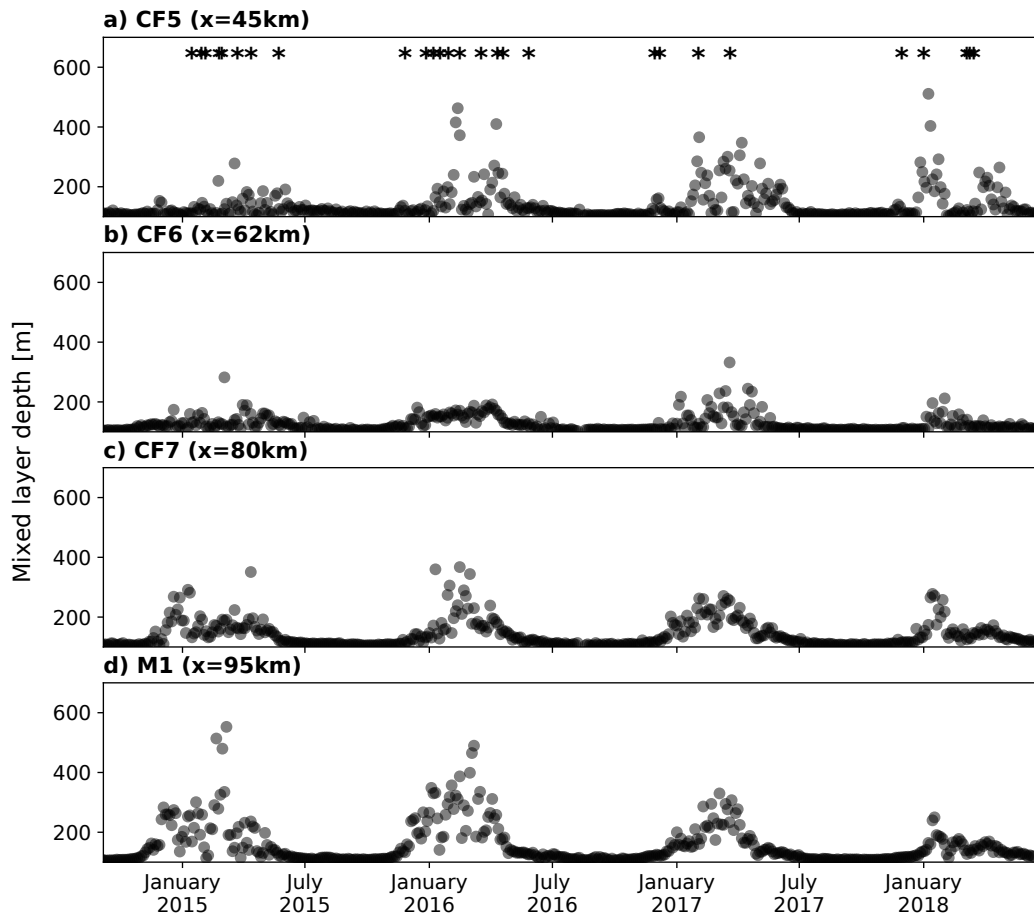


**Figure 7.** Three-day average vertical mixed layer depth calculated from mooring observations. Stars in panel a indicate down-front wind forcing events.

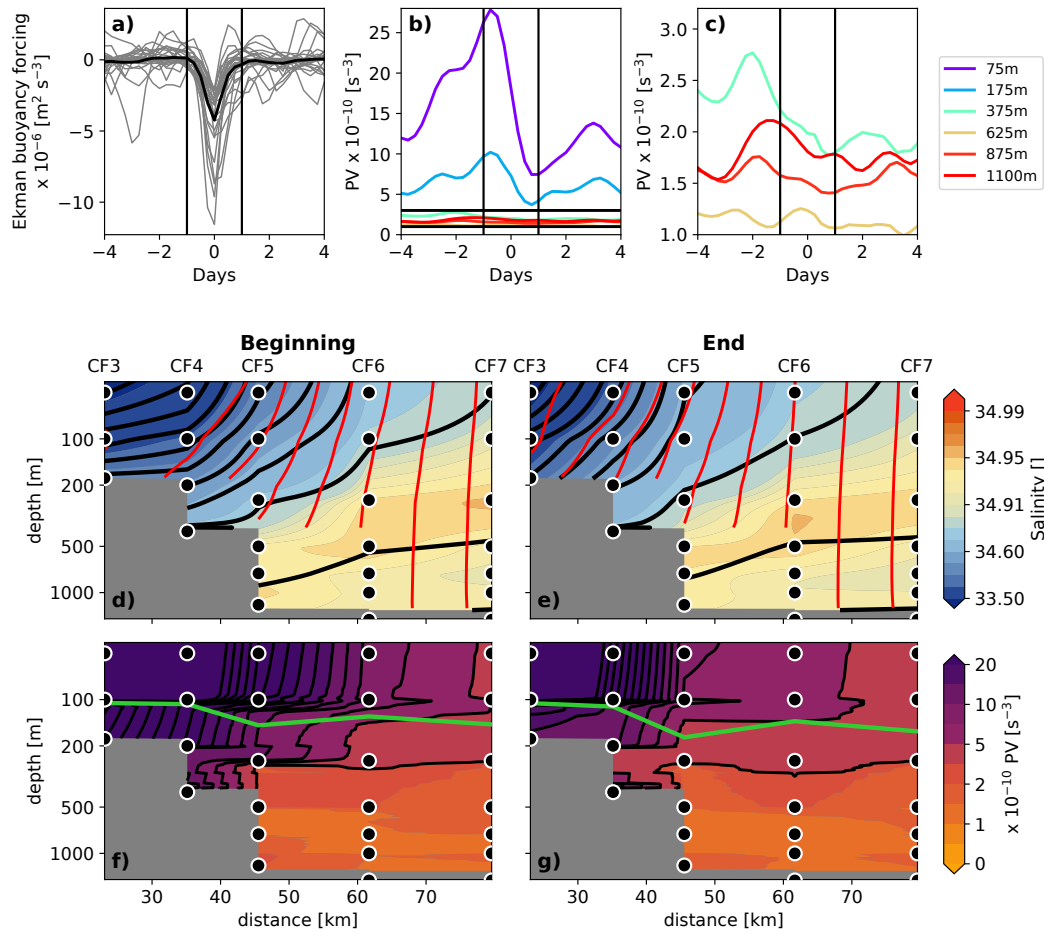


**Figure 8.** Evolution of a composite down-front wind event. **a)** Ekman buoyancy forcing during all slantwise convection events. The grey lines are all events, and the black line is the composite mean. **b)** Composite mean PV at the CF5 mooring between each of its instruments. The black horizontal lines indicate the range shown in panel c. The black vertical lines in panels a–c indicate the beginning and end of the composite event, which are the focus of panels d–g. **d, e)** Salinity, shown with  $\sigma_\theta$  isopycnals separated by  $0.1 \text{ kg m}^{-3}$  in black and zonal absolute momentum contours separated by  $1 \text{ m s}^{-1}$  in red. **f, g)** PV shown with black contours separated by  $2.5 \times 10^{-10} \text{ s}^{-3}$ , with an upper bound mixed layer depth estimate shown in green. Note that the vertical scale is logarithmic in panels d–g. Black circles indicate nominal moored instrument locations.

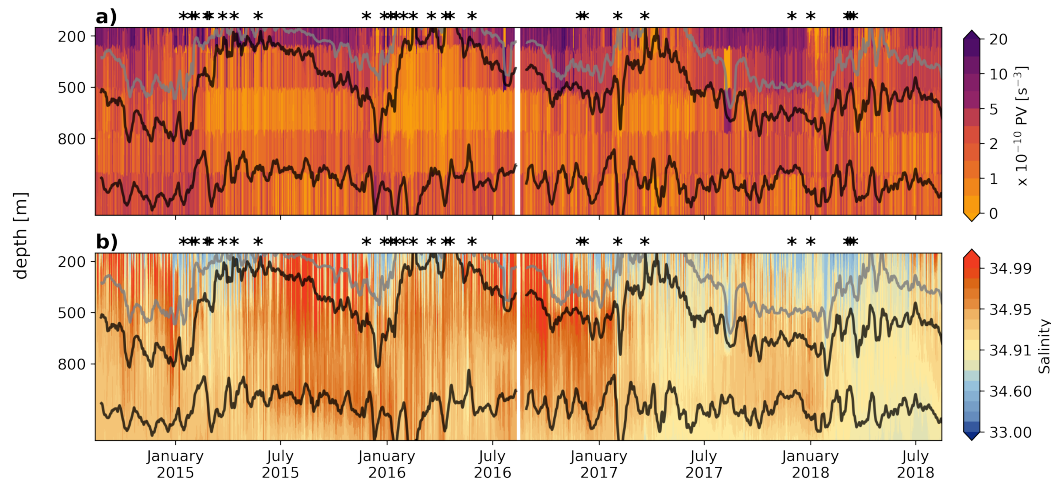


**Figure 9.** Temporal evolution of daily **a)** Potential Vorticity (PV) and **b)** salinity at the boundary current maximum (CF5). Black isopycnals mark the boundaries of upper ISIW,  $\sigma_\theta = 27.65 - 27.73 \text{ kg m}^{-3}$ ; the grey contour is the  $\sigma_\theta = 27.6 \text{ kg m}^{-3}$  isopycnal. Stars at the top of each panel indicate down-front wind forcing events.

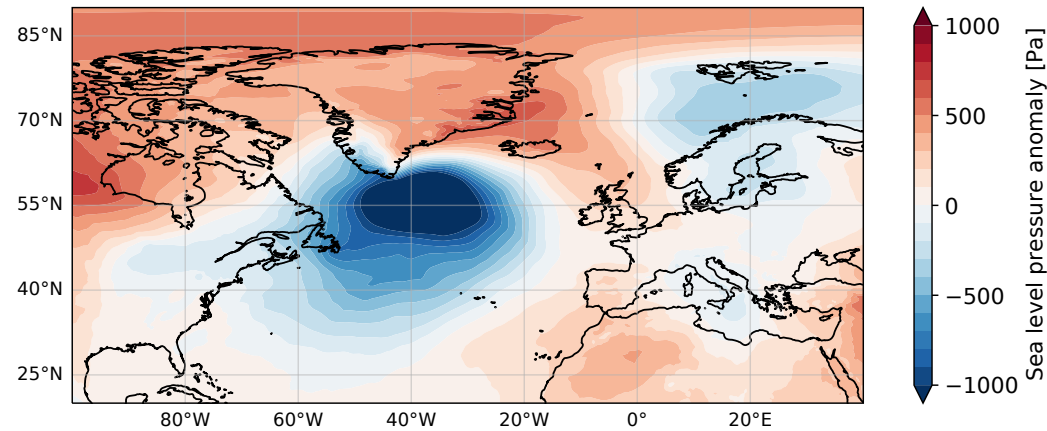


**Figure 10.** Composite of sea level pressure anomaly centered at the maximum Ekman buoyancy forcing at CF5. Anomalies are taken from the July 2014 – July 2018 time mean at each point.